Data processing pipeline for a time-sampled imaging Fourier transform spectrometer

David A. Naylor[*a], Trevor R. Fulton[a], Peter W. Davis[a], Ian M. Chapman[b], Brad G. Gom[a], Locke D. Spencer[a], John V. Lindner[a], Nathan E. Nelson-Fitzpatrick[a], Margaret K. Tahic[a] and Gary R. Davis[c]
[a]Department of Physics, University of Lethbridge, Lethbridge, Alberta, Canada
[b]Iunctus Geomatics Corp., Lethbridge, Alberta, Canada
[c]Joint Astronomy Centre, Hilo, Hawaii

ABSTRACT

Imaging Fourier transform spectrometers (IFTS) are becoming the preferred systems for remote sensing spectral imaging applications because of their ability to provide, simultaneously, both high spatial and spectral resolution images of a scene. IFTS can be operated in either step-and-integrate or rapid-scan modes, where it is common practice to sample interferograms at equal optical path difference intervals. The step-and-integrate mode requires a translation stage with fast and precise point-to-point motion and additional external trigger circuitry for the detector focal plane array (FPA), and produces uniformly position-sampled interferograms which can be analyzed using standard FFT routines. In the rapid-scan mode, the translation stage is continuously moving and interferograms are often acquired at the frame-rate of the FPA. Since all translation stages have associated velocity errors, the resulting interferograms are sampled at non-uniform intervals of optical path difference, which requires more sophisticated analysis. This paper discusses the processing pipeline which is being developed for the analysis of the non-uniform rapid-scan data produced by the Herschel/SPIRE IFTS.

Keywords: Imaging, Fourier, Transform, Spectrometer, Data Processing Pipeline, Herschel, SPIRE

1. INTRODUCTION

While multispectral imaging systems (i.e. those typically having ≤ 10, not necessarily overlapping, spectral channels), provide qualitative information on a scene, hyperspectral imaging systems, which can have many thousands of spectral channels, provide much more detailed information and allow for critical analyses of the scene contents. The applications of such systems are as diverse as astronomical imaging (star formation, galactic evolution, etc.), environmental monitoring (pollution in rivers, industrial plants, growth of illegal crops, etc.), earth observations from air/space (crop management, mineral composition, etc.), biomedical imaging (cell abnormalities, microscopy, etc.), counterfeit detection (art, money, etc.) and retinal imaging (security, glaucoma, etc.) to name a few[1,2,3]. In each case the resulting spectral data cube or hypercube is analyzed by comparison to reference spectral templates, to study such things as a galaxy's red shift, a cell's DNA or a counterfeit currency.

Fourier transform spectroscopy (FTS) is the most widely used technique for retrieving spectral information of physical systems at infrared wavelengths. The advantages of Fourier spectroscopy over competing techniques are legendary: high throughput (Jacquinot advantage), simultaneous measurement of all wavelengths (multiplex or Felgett advantage), intrinsic wavelength calibration and the best instrumental line-shape of any spectrometer (Connes advantages)[4]. The principal disadvantage is the sensitivity of the technique to fluctuations in the source intensity. Since FTS is a multiplexing technique in the time-domain, any temporal variations in the signal result in spectral features in the computed spectrum; this is particularly problematic for periodic source fluctuations, which result in narrow spectral noise features. A second disadvantage of the technique is the complexity of the mathematical methods required to compute the spectrum.

---

[*] naylor@uleth.ca; phone 1-403-329-2426; fax 1-403-329-2057; www.uleth.ca/phy/naylor/

2. BACKGROUND

A Fourier transform spectrometer is a two-beam interferometer, shown schematically in Figure 1. The incident beam is first collimated and subsequently divided into two beams of equal intensity by a beamsplitter. After reflection from a fixed and a moving mirror, the beams recombine at the beamsplitter and are brought to a focus on the detector. The signal recorded by the detector as a function of the optical path difference (OPD) between the recombining beams, z, is known as the interferogram, $I(z)$. Ideally, this signal would possess even symmetry, and could thus be expressed as the cosine Fourier transform of the incident radiation field, $B(\sigma)$. However, in practice, wavelength dependent phase, $\phi(\sigma)$, is unavoidably introduced and the interferogram takes the form:

$$I(z) = \int_{-\infty}^{+\infty} B(\sigma) \exp(i\phi(\sigma)) \exp(2\pi i z \sigma) \, d\sigma \qquad (1)$$

Inversion of this equation, duly accounting for the effects of finite optical path, discrete sampling interval and phase errors associated with optical and/or electronic components, allows the spectrum to be recovered[4,5,6].

By virtue of its axial symmetry, the FTS falls into the class of spectrometers possessing the highest throughput, typically exceeding that of a grating spectrometer by two orders of magnitude for beamsplitters and diffraction gratings of the same size. By measuring all spectral components simultaneously, the FTS gains a multiplex advantage over a grating spectrometer in the case where the detector is the limiting noise source. While improvements in detector technology, in particular focal plane arrays (FPA), are reducing this gain, the FTS retains key advantages of high throughput, rigorous wavelength calibration, and well-defined instrumental line-shape. Moreover, as shown in Figure 1, since the image plane of the FTS is a stigmatic replica of the object plane, a detector array placed at the output of the FTS enables imaging spectroscopy, thus exploiting both spectral and spatial multiplexing. A real object or an image formed by additional foreoptics (e.g., a telescope or microscope) can be located at the object plane. If desired the collimating optic can be removed altogether and the imaging FTS (IFTS) views infinity. For the above reasons IFTS are becoming the choice spectrometer for many remote sensing applications.
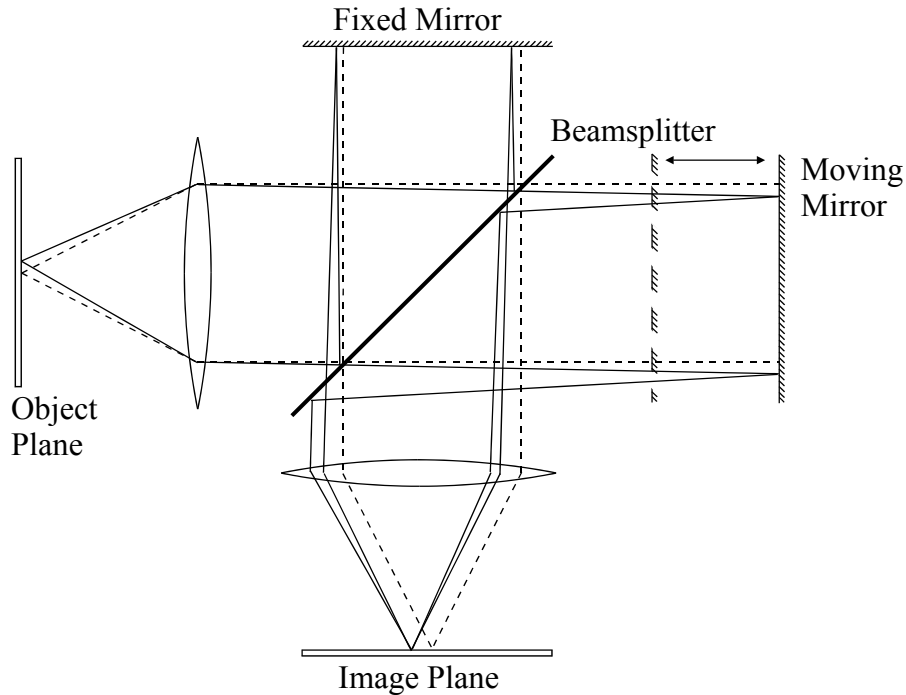

Figure 1 A schematic of an imaging Fourier transform spectrometer.

3. HERSCHEL/SPIRE

Herschel is the fourth cornerstone mission in ESA's Horizon 2000 scientific program[7]. It is scheduled for launch in February 2007 with a planned lifetime of 4 years at the Sun-Earth L2 Lagrangian point. Herschel is designed to provide imaging photometry and spectroscopy over the relatively unexplored spectral range 80–670 μm, and will provide unprecedented submillimetre sensitivity, enabling astronomers to explore some of the most fundamental questions of modern astrophysics:

- the statistics and physics of galaxy formation at high red shift,
- the statistics and physics of star formation in our own and nearby galaxies,
- study of the interaction between stars and the interstellar medium at all stages of the stellar life cycle,
- formation and evolution of the solar system.

One of the three instruments of the Herschel payload is the Spectral and Photometric Imaging Receiver (SPIRE), which will provide photometry and spectroscopy over the spectral range 200–670 μm using bolometric detector arrays. The detector arrays are constructed from feedhorn-coupled "spider-web" NTD germanium bolometers which are cooled to 300 mK by a ^{3}He-^{4}He closed cycle refrigerator. SPIRE's spectrometer is an IFTS of the Mach-Zehnder design and uses novel broadband intensity beam dividers to provide high efficiency with spatially separated input and output ports[8]. One input port covers a 2.6-arcminute diameter field of view on the sky and the other is fed by an on-board blackbody reference source designed to null the interferometric modulation from the continuum radiation emitted by the Herschel telescope. Two bolometer arrays, covering the spectral ranges 200-325 μm and 315–670 μm, are located at the output ports. The IFTS moving mirror drive mechanism can be operated in either rapid-scan or step-and-integrate mode. The spectral resolution is adjustable between 0.04 and 2 cm^{-1} (corresponding to resolving powers, $\lambda/\Delta\lambda$, of 1000–20 at 250 μm, respectively). In order to reduce the complexity of the hardware, the read-out electronics for the mirror drive mechanism and the bolometer arrays operate independently of one another, which means that it is impossible to read-out the detector signal at equal intervals of OPD. This requires sophisticated post-processing of the independently, time-sampled, OPD and detector signals, which is described below. Details of the SPIRE design are given elsewhere[9,10].

4. DATA PROCESSING MODULES

Fourier transform spectrometers have the advantage of relatively simple optical and mechanical design, but the disadvantage of requiring complex data reduction software. IFTS systems present an increased processing burden that is proportional to the number of pixels in the FPA. The following sections describe the key software modules for the data processing pipeline for a time-sampled IFTS. In addition to these, modules exist to allow for quality inspection of the interferograms, wavelength scale correction for off-axis pixels (the obliquity effect in IFTS), inspection of the resulting spectral data cubes, and standard spectral processing (average, difference, ratio, etc).

4.1. Deglitching cosmic ray events

When cosmic rays strike a sensitive bolometer, they impart such energy that the bolometer is abruptly perturbed from its normal operating point, returning to it with a time constant that is characteristic of the thermal conductivity of the link between the bolometer and its thermal sink, and of the electrical filter characteristics of the detector electronics. Such events are particularly problematic in Fourier spectroscopy as they occur in the time-domain and introduce sinusoidal noise components across the whole spectrum upon transformation.

While manual procedures for the identification and removal of cosmic ray events from FTS data are practical for single-pixel detector systems, they become impractical for imaging systems. An automated deglitching scheme, which exploits the knowledge of the time constant of the detector and its associated electronics must be implemented. A variety of deglitching schemes can be devised. The optimal deglitching scheme should find very small cosmic ray signatures without flagging any false positives. The zero path difference (ZPD) region of the interferogram is the most challenging one in which to detect cosmic ray events, since it is here that the interferogram experiences its greatest modulation, which causes a slope discriminant algorithm to fail. We have adopted a two tier approach. Near the ZPD region, several interferograms of the same source are used to establish a mean to which individual interferograms are compared statistically to identify glitches; this does not require high resolution data and therefore requires only a reasonable

amount of time. Far from the ZPD region, a slope discriminant algorithm is used. Once identified, the glitches can be removed by simple linear interpolation between the point immediately before the event and one a given number of time constants later. Techniques based on wavelet analysis have been proposed, however, these break down at sampling rates close to the Nyquist frequency[11]. More sophisticated approaches attempt to retrieve the modulation superimposed on the exponential decay component of the signal[12], but this is complicated by changes in detector responsivity as a function of detector temperature.

Finally, because the interferogram data are sampled in equal intervals of time, it is possible for the glitch detection algorithm to use the fitted time constant of a suspected cosmic ray event as a quality flag for the event. Figure 2 shows data from the BLAST experiment[13] in which our algorithm has detected two potential cosmic ray events. The BLAST data were chosen for analysis because BLAST employs the same detector arrays as SPIRE. Upon closer examination, one event shows the asymmetric signature of a cosmic ray impact, with a steep slope in the observed signal followed by an exponential decay to the mean signal value, while the other has a more symmetrical profile typical of an astronomical source. These differences can be used to develop algorithms that can discriminate cosmic ray events from astronomical sources.
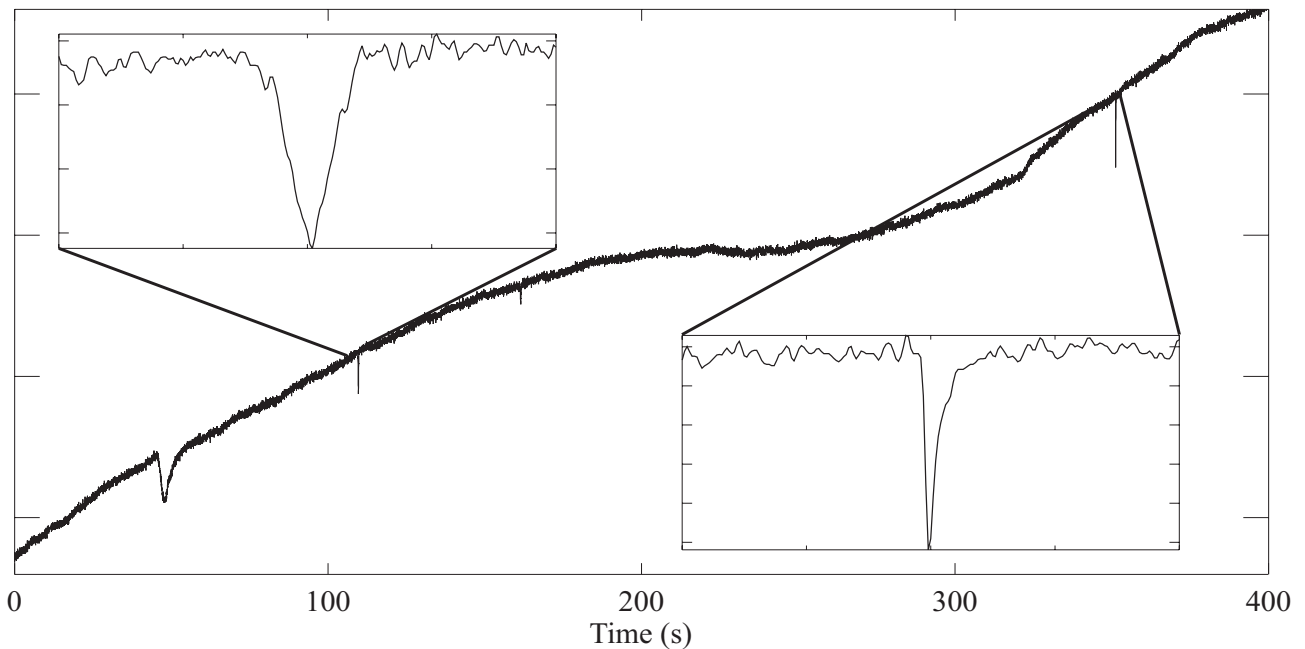

Figure 2. Data obtained with a BLAST bolometer detector array showing the identification of a real and false cosmic ray event. The zoomed windows, each 2 seconds in length, represent a small fraction of the astronomical data stream.

4.2. Phase correction
Phase correction is necessary to extract the maximum amount of information from the interferogram[4]. In addition to the linear phase error associated with not sampling the interferogram precisely at the ZPD position, phase errors can be introduced by the optical elements of the spectrometer, the detector and its electronics. When these additional contributions introduce negligible dispersion over the spectral range of interest, a linear phase correction function can be computed (by weighting phase values obtained from a short, double-sided interferogram by the square of the magnitude of the corresponding spectral point) and convolved with the interferogram (deglitched if necessary) to produce a phase-corrected interferogram[6]. Non-linear phase errors require more sophisticated treatment, usually by fitting a weighted polynomial function to the measured phase data, or by fitting a function derived from a theoretical model.

4.3. Apodization

With an FTS the opportunity exists to modify the instrumental line shape (ILS) in post processing by the use of apodization functions. The goal of apodization is to reduce the side-lobes at the expense of lowering the spectral resolution. Many apodizing functions have been reported in the literature and practitioners often make their choice without a clear understanding of the role of the function on the independence of the resulting spectral data points. While purists would question the need for apodization, the reduction in the amplitude of the secondary maxima of the ILS, albeit at the cost of lower spectral resolution, is often desired.

We have extended the work of Norton and Beer[14] to generate a family of apodizing functions that are close to optimum, in the sense that, to a large degree, they preserve the orthogonal properties of the sinc function, provide near optimum reduction in the amplitude of secondary maxima for a given decrease in spectral resolution, and are simple to compute[15]. The left plot in Figure 3 shows the ILS for the 10 apodizing functions which correspond to increases in the full width of the ILS between 1.1 and 2.0 in steps of 0.1 in comparison to the unapodized sinc ILS (shown as a dotted line). The right plot in Figure 3 shows the location of these ILS functions on the Filler diagram[16], which graphs the height of the absolute largest secondary lobe of the ILS (normalized with respect to the height of the main lobe) relative to the absolute height of the largest secondary lobe of the sinc function, as a function of the full width at half maximum (FWHM) of the ILS, again relative to the FWHM of the sinc function. The solid curve on this plot is the empirically determined optimum boundary[14]. Also shown on this plot is the location of the frequently used, yet far from optimum, triangular apodizing function.
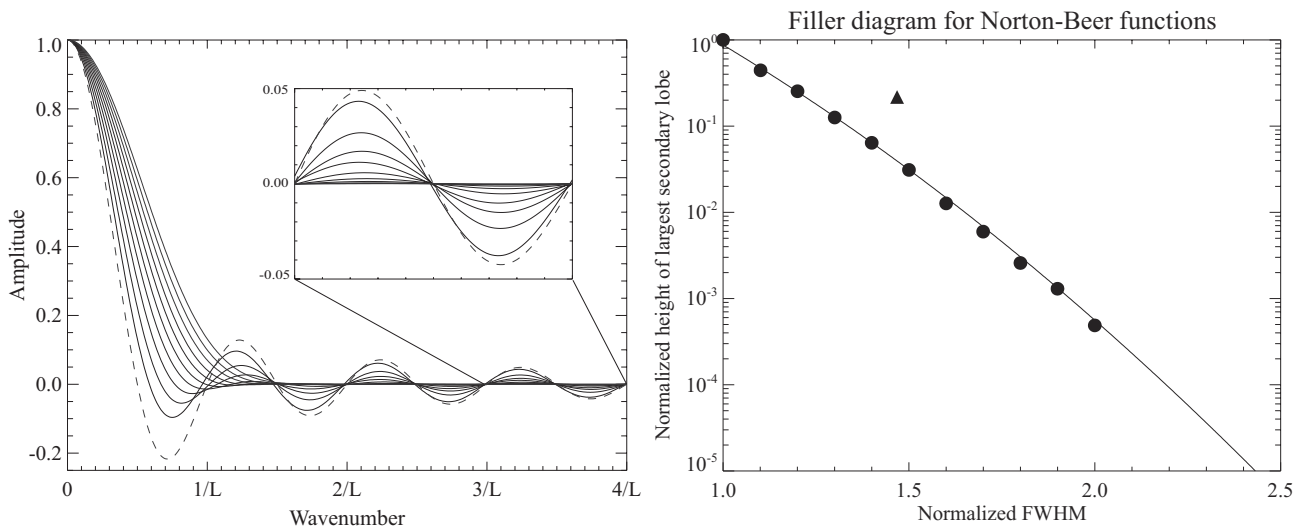

Figure 3. Instrument line shapes (left) corresponding to optimum apodizing functions plotted on the Filler diagram (right). Line shapes have FWHM ranging from 1.0 to 2.0 in steps of 0.1. The location of the triangular apodizing function is shown for comparison; the solid line is the empirically determined optimum boundary[14].

4.4. Fourier transformation

IFTS can be operated in two modes: step-and-integrate (SI) and rapid-scan (RS). In the SI mode, the OPD in the interferometer is incremented in equal steps and the FPA is read out in a snapshot mode when the interferometer mirrors are stationary. The SI mode requires that the translation stage is capable of fast and accurate point-to-point moves. Since the resulting data cube (consisting of two spatial and one optical path dimensions) is sampled in equal OPD steps, the spectrum can be obtained from inversion of equation 1 by using the FFT algorithm[17].

In the RS mode, the moving mirror of the interferometer is scanned at constant velocity, and some form of metrology (e.g., laser, capacitance micrometry, Moiré encoder) is required to sample the interferogram, usually on a uniform OPD grid. When interferograms are sampled on a uniform time grid, however, (as is the case for the SPIRE instrument[9], most

systems employing delta-sigma analog-to-digital converters[18] and time-synchronized readout electronics of FPAs) account must be taken of the fact that no translation stage can maintain perfectly constant velocity. As a result, equal intervals in time do not correspond to equal intervals in OPD and this introduces a sampling position error into the interferogram, which generally has both random and periodic components. Unless these sampling errors are corrected, the derived spectrum will exhibit ghosts on either side of the true spectrum; the relative strength of these ghosts being proportional to the amplitude of the periodic sampling error[18].

The hardware required for the control and data acquisition system of an IFTS can be greatly simplified by reading out the FPA and the mirror stage position at independent times. In such a time-sampled FTS, the interferogram, $I(t)$, is measured at time, t, while the OPD, $z(t')$, is measured at a different time, t'. In the case of an IFTS, individual pixels are frequently read out sequentially as determined by the multiplexing scheme (e.g., $I_0(t)$, $I_1(t+\Delta t)$,…, $I_n(t+n\Delta t)$), but the analysis remains the same. The problem reduces to one of merging $I(t)$ and $z(t')$ to form $I(z)$, which is subsequently Fourier transformed to produce the spectrum. In general $I(z)$ will not be regularly gridded in OPD. Below we discuss two methods of computing the Fourier transformation of time-sampled data from an FTS: interpolation followed by an FFT and an iterative scheme using the non-uniform FFT. In section 5 we compare the effectiveness of these methods on simulated data.

4.4.1. Interpolation and FFT

The interpolation scheme is shown in Figure 4. The time-sampled OPD data, $z(t)$, are fitted with a natural cubic spline, which is then evaluated on the uniform OPD grid, x_i, to determine the desired times, t_i'', at which the interferogram measurements are required. Brault has devised an elegant scheme to evaluate $I(t'')$ by convolving $I(t)$ with the effective digital filter response of the interferometer, the continuous sinc function, which is multiplied by a Gaussian function to minimize spectral artifacts caused by the finite truncation of the sinc function[18]. A second order correction modifies the digital filter to take into account the fact that the sinc function is appropriate for interpolating data taken uniformly in OPD, and not in time. Brault also discusses how to account for the effects of velocity variations on the frequency dependent amplitude and phase response of the detector and electronics. In the analysis presented here we have taken an even simpler approach and compare three interferogram interpolation schemes, linear, second order polynomial and cubic spline, to reconstruct $I(t'')$ from $I(t)$. Elsewhere, the cubic spline interpolation has been shown to be slightly superior to the more complex first order correction of Brault[19]. The fast Fourier transform algorithm[17] can then be invoked to compute the spectrum of the regularly sampled interferogram, $I(x)$.
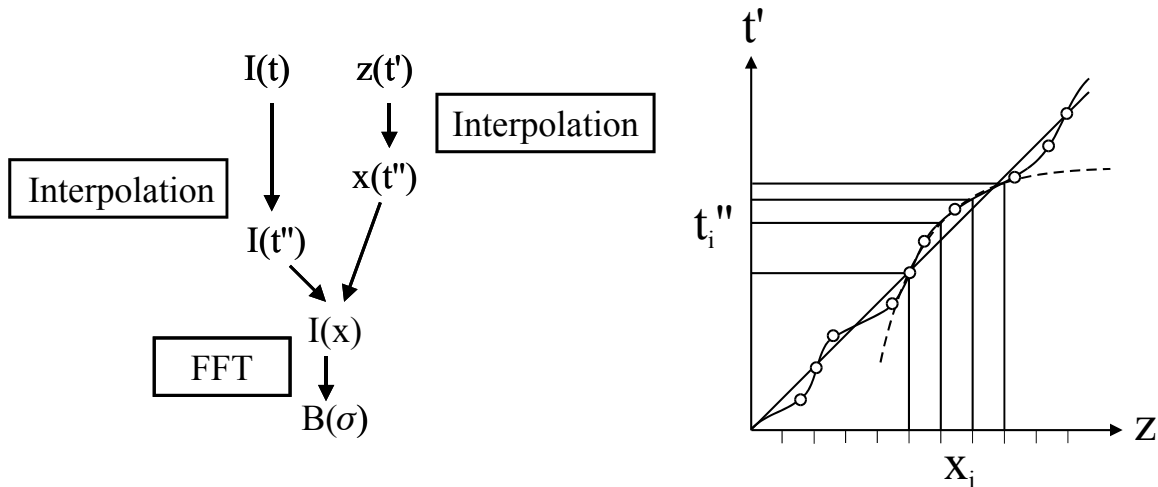

Figure 4. A flow chart of the interpolation scheme and a graph illustrating how the times, t_i'', corresponding to equal increments of OPD, x_i, are determined from spline fitting to the OPD-time data.

4.4.2. Non uniform FFT (NFFT)

The non-uniform discrete Fourier transform (NDFT) can be calculated directly from:

$$B(m\Delta\sigma) = \sum_{n=1}^{N} I(z_n)\exp(-im\Delta\sigma z_n) \qquad m = -M/2 .... \ M/2 - 1 \qquad (2)$$

where, $B(m\Delta\sigma)$, is the spectral amplitude at wavenumber $m\Delta\sigma$, and $I(z_n)$ is the irregularly spaced interferogram. The non-uniform fast Fourier transform algorithm (NFFT)[20] provides an efficient means of evaluating equation 2. Since the NFFT algorithm is approximate by nature, iterative methods have been devised in an attempt to improve this approximation[21]. An iterative NFFT (iNFFT) software package is currently under development[22]. This package offers the choice of four efficient iterative schemes including the conjugate gradient and steepest descent minimization methods.

The NFFT method is shown schematically in Figure 5. The OPD-time data, z(t), are fitted with a natural cubic spline, which is then evaluated on the uniform time grid, t_i, to determine the corresponding OPD values, z_i', at which interferogram data exist. The two data sets are then combined to form I(z') which is then input to the iNFFT.
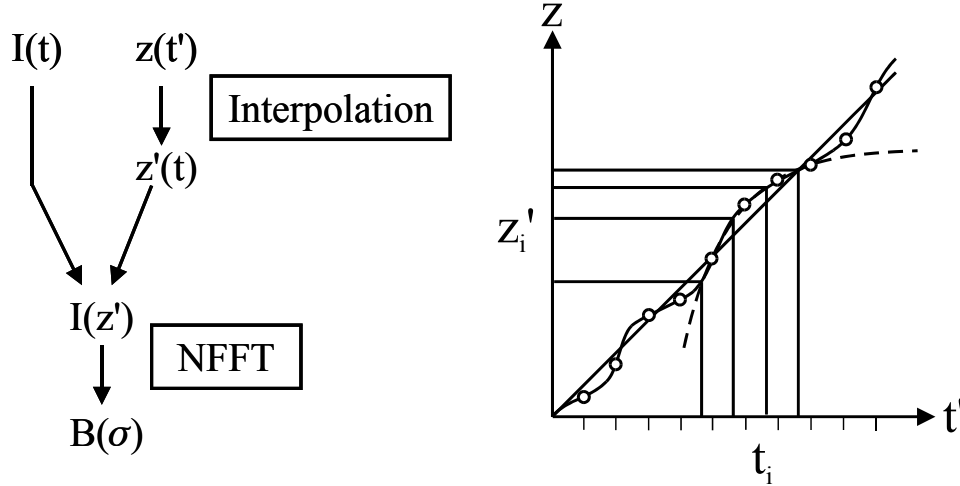

Figure 5. A flow chart of the nonuniform Fourier transform scheme and a graph illustrating how the OPD positions, z′(t), are determined from curve fitting to the OPD-time data.

Each iNFFT algorithm involves both forward and reverse non-uniform FFT subroutines. The forward NFFT subroutine transforms an irregularly sampled N-point signal, $I(z_n)$, in the spatial domain to a regularly sampled M-point signal in the spectral domain. The N-point signal in the spatial domain is first resampled onto a regular grid of n points (where n is a power of 2 greater than N) by way of a convolution with a window function, ψ. This resampled signal is then transformed to the spectral domain with the familiar FFT. Finally, the effect of over-sampling in the spatial domain is removed by truncating the resultant spectrum to M points and the effect of the convolution is removed by deconvolution of the truncated result with an equivalent spectral domain window function, φ. This reduces the spectral band to the width of the window function and reduces the spectral resolution to M points.

For the reverse NFFT, the first step is to deconvolve the M-point spectral domain function with the equivalent spectral domain window function, φ. The deconvolved result is then zero-padded to n spectral elements (where n is again a power of 2 greater than N). A reverse FFT is applied to the zero-padded spectrum, resulting in a finely sampled n-point interferogram. This interferogram is then resampled onto the original sparser, irregularly sampled N-point grid, by way of convolution with the spatial domain window function, ψ. It is of note that interpolating the interferogram by convolution with a window function is equivalent to the approach taken by Brault. Various window functions have been used in the literature, including the combination of Gaussian and sinc kernels[23], as used by Brault[18].

As mentioned above, the iNFFT software package provides for four different iterative methods for transforming irregularly sampled interferograms. The structure of each iterative scheme is similar in that they each consist of an initialization phase followed by an iterative phase. Moreover, while the procedures of the iterative methods may differ slightly, they are each based on a general principle; the comparison between the inverse transform of the derived output spectrum and the original interferogram. By way of example, consider the steepest descent method. The initialization phase begins with an initial guess at the output spectrum. The inverse transform of this initial guess is subtracted from the original interferogram, the result of which is the initial residual interferogram. The forward transform is then applied to the residual interferogram, giving rise to an initial residual spectrum. The iterative process then begins. For each iteration, a new residual interferogram is computed by subtracting the inverse transform of residual spectrum of the preceding iteration from the previous residual interferogram. The forward transform of the newly calculated residual interferogram then becomes the new residual spectrum and is added as a correction to the derived output spectrum. For well-conditioned systems, the residual interferogram (as well as its residual spectrum transform) will decrease in magnitude with each iteration. Suitable convergence criteria based on the magnitude of the residual interferogram or on the magnitude of the correction that is applied to the derived output spectrum can be used to terminate the iterative process.

5. RESULTS

5.1. Synthetic interferograms

In order to compare and contrast the interpolation and iNFFT methods simple spectra, limited to the wavenumber range 30–50 cm^{-1} (corresponding to one of the SPIRE spectrometer bands[9]), were zero-infilled and Fourier transformed to produce highly oversampled *master* interferograms. The master interferograms provide regularly-sampled signal and position arrays, with properties shown in Table 1. Two test spectra were studied. The first consisted of a single resolved Gaussian line of unit amplitude, centered at 40 cm^{-1}, and having a FWHM of 0.2 cm^{-1}. The second spectrum consisted of a linear combination of a flat continuum of unit amplitude spanning the region 30 to 50 cm^{-1}, a Gaussian absorption line of amplitude 0.5, centered at 40 cm^{-1}, having a FWHM of 0.2 cm^{-1}, and an unresolved emission line of unit amplitude also centered at 40 cm$^{-1.}$

Interferogram data points	2^{20}
OPD range	-12.5 to +12.5 cm
Stage velocity	1.0 mm/s
Sampling rate	4.1943 kHz
Nyquist frequency	20971.52 cm^{-1}
Signal band	0 - 50 cm^{-1}
Spectral Resolution	0.04 cm^{-1}
Translation stage sub-sampled rates	40, 80, 160 Hz
Detector sub-sampled rates	10, 20, 40 Hz
Sub-sample Nyquist frequencies	50, 100, 200 cm^{-1}

Table 1. Properties of the master interferograms.

The time-sampled position values of the master interferograms were modified to generate non-uniformly sampled position arrays by the introduction of simulated velocity variations, or jitter, in the interferometer translation stage. The jitter includes a 1/f noise component and a resonance at 15 Hz, which simulates a servo-loop tracking error. To generate the 1/f noise, a random white noise array was first generated, Fourier transformed, and the resultant noise spectrum multiplied by 1/f. The inverse Fourier transform of the noise spectrum was then calculated and scaled to contribute the desired level of jitter, expressed as an RMS. The sinusoid noise component was set equal to the RMS velocity noise from the 1/f component. Figure 6 shows the variation in velocity, and the corresponding noise spectrum, for the case of 10% RMS total jitter. Velocity jitters of 5, 10, 15, 20, and 25% have been considered in the following analysis.

When the resulting motion was sampled in equal time intervals, the varying velocity shown in the left graph of Figure 6 was used to generate irregularly spaced position arrays. To simplify the analysis, it was arranged to sample the zero path difference position so that no linear phase errors were introduced. Once the irregular position arrays were created, the master interferogram arrays were sub-sampled to the detector and stage time-sampling intervals given in Table 1. This results in separate signal-time, $I(t)$, and position-time, $z(t')$, data-sets for each test spectrum, which were then processed by the interpolation and iNFFT algorithms discussed above. In practice for any given total velocity jitter 100 sub-sampled interferograms, each derived from an independent and random velocity jitter distribution, were generated from the master interferogram in order to ensure randomness in the analysis.
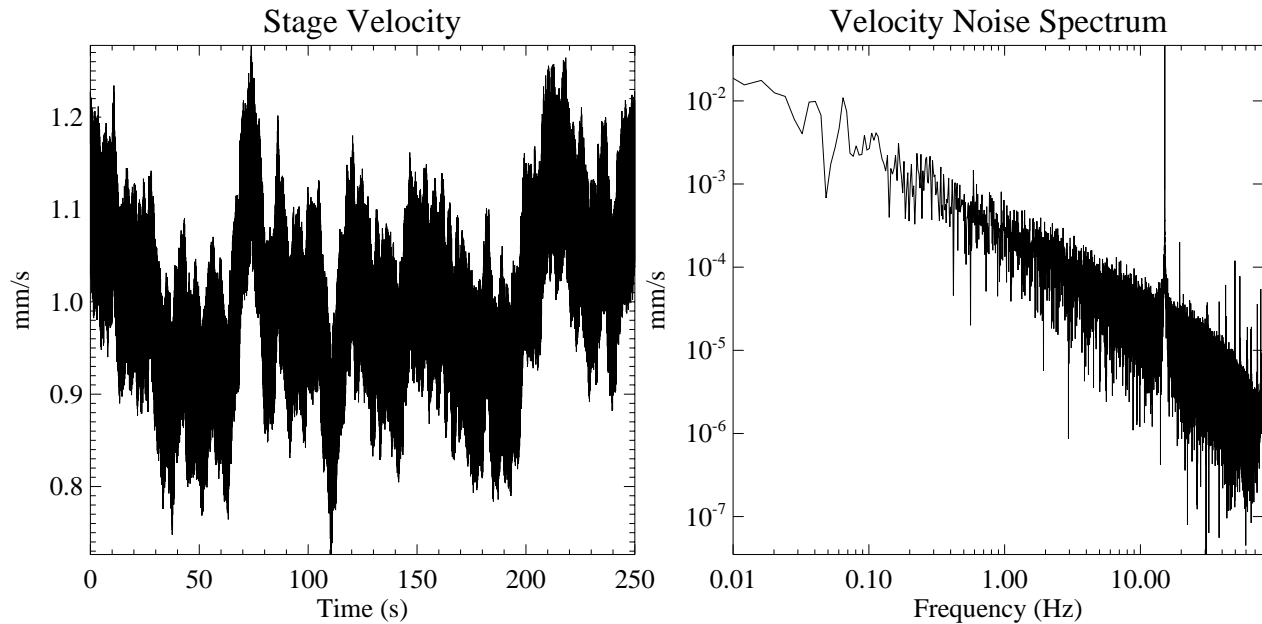

Figure 6. Simulated stage velocity (left) and corresponding velocity noise spectrum (right) for a stage having a nominal velocity of 1.0 mm/s with an RMS jitter of 10% split evenly between a sinusoidal resonance at 15 Hz and the rest of the spectrum.

5.2. Analysis of resolved Gaussian line

Figure 7 shows the results obtained for the three interpolation methods and the iNFFT method applied to the spectrum of the single resolved Gaussian line described above, sampled such that the Nyquist frequency was 50 cm^{-1}. The four graphs show the errors in the retrieved values of the amplitude, FWHM and area of the Gaussian line and the total spectral RMS, as a function of analysis method and velocity jitter. The retrieved values were obtained using the IDL[24] GAUSSFIT function[25]. All values are shown as percentages of the true value, with the exception of RMS error which is shown as a percentage of the line amplitude. The curves shown represent the mean of 100 test trials, having the same total, but different random, velocity jitter. Three principal results emerge: in all methods the error increases as a function of the velocity jitter; of the interpolation methods the spline is superior to both the linear and second order methods; and in all cases the iNFFT method is superior to interpolation methods.
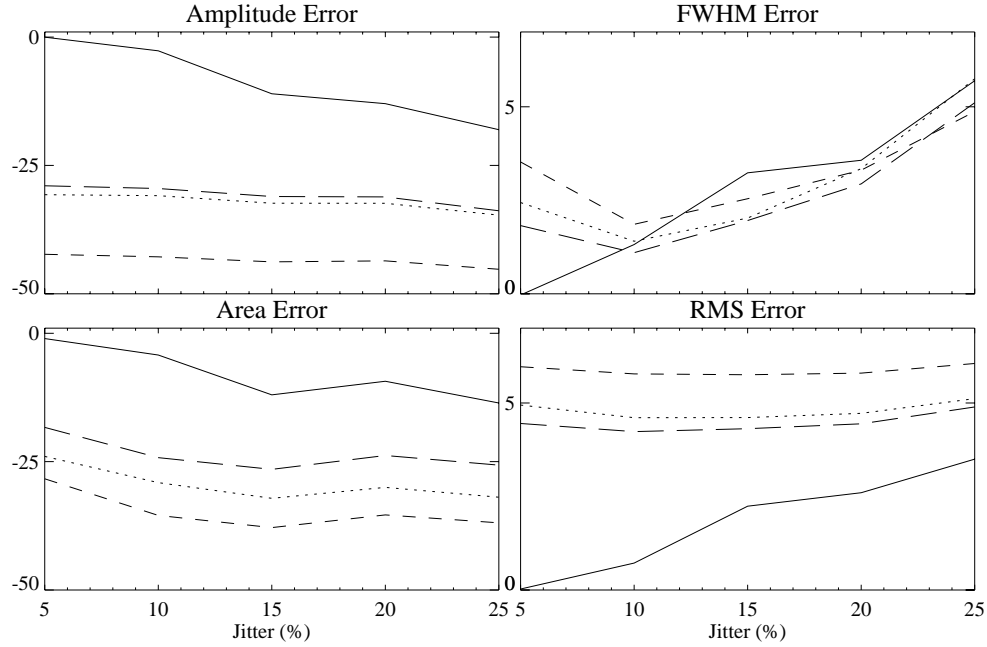
Figure 7. Amplitude, FWHM, area and RMS error determined from linear (short dash), second order polynomial (dotted) and natural cubic spline (long dash) interpolation + FFT method, and the iterative NFFT (solid line) method, expressed as a percentage, as a function of total velocity jitter expressed in RMS.

5.3. Analysis of compound spectrum

The analysis of section 5.2 was extended to study the more realistic and complex spectrum consisting of the linear combination of a continuum emission component, a resolved Gaussian absorption line and an unresolved emission line, described in section 5.1. Given its superior performance, in this analysis, only the spline interpolation method was compared with the iNFFT method. The results are shown in Figure 8 for a 10% RMS velocity jitter. The upper two graphs correspond to interferograms sampled such that the Nyquist frequency was 50 cm^{-1} (i.e. marginally oversampled) the lower two graphs correspond to interferograms sampled such that the Nyquist frequency was 100 cm^{-1} (i.e. twice oversampled). The right hand graphs show a magnified region around the Gaussian line centre. Component spectral parameters have been determined from the retrieved spectra using the IDL[24] MPFITFUN function which, given the expected functional form of the spectrum, uses the Levenberg-Marquardt least squares method[26] to fit to the data. The derived spectral parameters are given in Table 2. It can be seen that in the oversampled case both methods yield results which are in good agreement with the input spectrum, however, in the marginally sampled case the iNFFT yields superior results.

	Original	NFFT(σ_N=50 cm^{-1})	NFFT (σ_N=100cm^{-1})	Spline (σ_N=50 cm^{-1})	Spline(σ_N=100 cm^{-1})
Continuum Amplitude	1.0	0.993 ± 0.003	1.000 ± 0.003	0.916 ± 0.002	1.007 ± 0.003
Resolved line center (cm-1)	40.0	40.002 ± 0.001	40.000 ± 0.001	40.001 ± 0.001	40.000 ± 0.001
Resolved line amplitude	-0.5	-0.457 ± 0.005	-0.501 ± 0.006	-0.344 ± 0.006	-0.492 ±.006
Resolved line FWHM (cm-1)	0.2	0.215 ± 0.003	0.200 ± 0.003	0.195 ± 0.004	0.200 ± 0.003
Unresolved line center (cm-1)	40.0	39.9999 ± 0.0002	40.0000 ± 0.0002	40.0004 ± 0.0002	40.0000 ± 0.0002
Unresolved line amplitude	1.0	0.98 ± 0.02	1.00 ± 0.02	0.70 ± 0.01	0.99 ± 0.02

Table 2. Retrieved spectral values and their errors for the resolved and unresolved components of the combination spectrum shown in Figure 8.

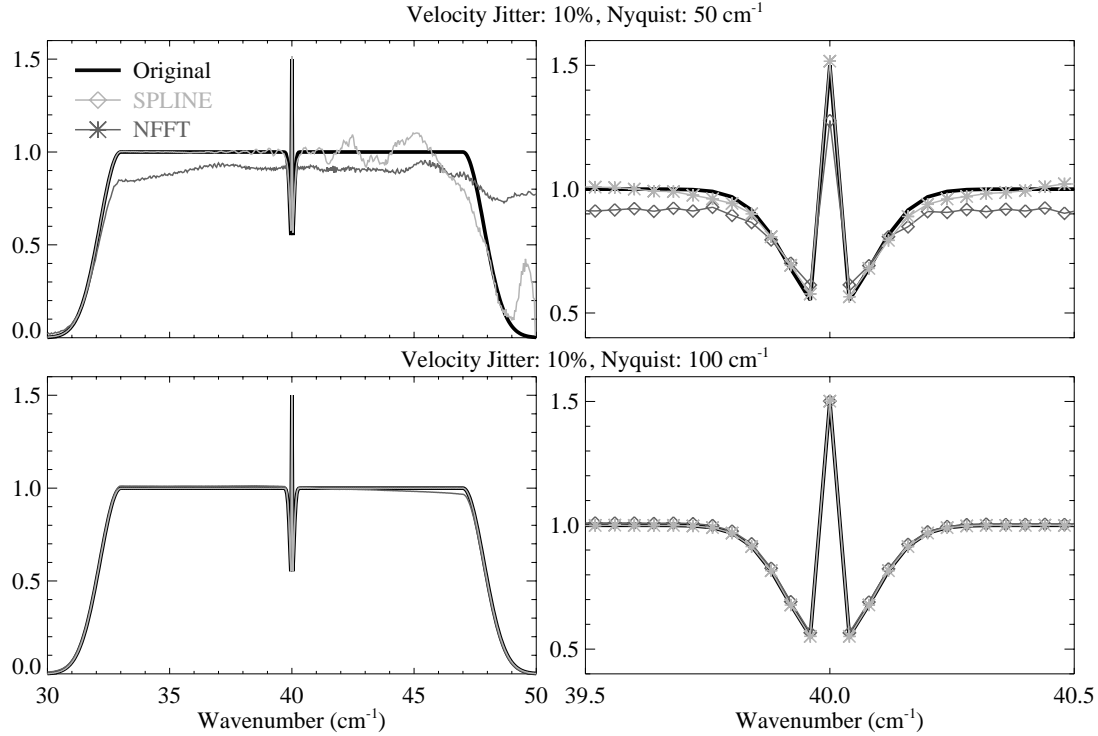Velocity Jitter: 10%, Nyquist: 50 cm^{-1}

Figure 8. A comparison of the retrieved spectra to the original combination spectrum (solid line) for the NFFT (light gray and *) and spline interpolation (dark gray and ◊) for the case of a 10% velocity jitter and Nyquist frequencies of 50cm-1 (upper graphs) and 100cm^{-1} (lower graphs).

6. CONCLUSIONS

In this paper, we have discussed the key software modules for the data processing pipeline of a time-sampled imaging Fourier transform spectrometer. Two approaches have been explored for the complex task of retrieving spectral information from interferograms sampled on a non-uniform OPD grid. The iterative NFFT method has been shown to produce superior results to classical interferogram interpolation schemes and is particularly powerful in the case of modest oversampling of data obtained with typical velocity jitter of ~10%. In this paper we have been primarily concerned with accuracy and not computation speed, however, convergence typically occurs in ~5 iterations, making spectral retrieval by this method practical with modern PCs. Since the iNFFT shares similarities with Brault's method[18], we are planning to merge the two schemes by using a sinc-Gauss kernel of window functions.

ACKNOWLEDGEMENTS

REFERENCES

1. Colarusso, P., Kidder, L.H., Levin, I.W., Fraser, J.C., Arens, J.F. and Lewis, E.N., *Infrared spectroscopic imaging: From planetary to cellular systems*, Applied Spectroscopy, **52**, 106A-120A, 1998.

2. Koenig, J.L. and Snively, C.M., *Fast FT-IR imaging: Theory and applications*, Spectroscopy, **13**, 22-28, 1998

3. Schultz, C.P., *The potential role of Fourier transform infrared spectroscopy and imaging in cancer diagnosis incorporating complex mathematical methods*, Technology in Cancer Research and Treatment, **1**, 95-104, 2002.

4. Davis, S.P., Abrams, M.C. and Brault, J.W., *Fourier Transform Spectrometry*, Academic Press, 2001.

5. Bell, R.J., *Introductory Fourier Transform Spectroscopy*, Academic Press, New York, 1972.

6. Forman, M.L., Steel, W.H. and Vanasse, G.A*., Correction of asymmetric interferograms obtained in Fourier spectroscopy*, J. Opt. Soc. Am., **56**, 59-63 ,1966.

7. http://astro.estec.esa.nl/herschel/

8. Ade, P.A.R., Hamilton, P.A. and Naylor, D.A., *An Absolute Dual Beam Emission Spectrometer*, Fourier Transform Spectroscopy: New Methods and Applications, OSA, 90-92, 1999.

9. Swinyard, B.M., Ade, P.A..R., Griffin, M.J., Dohlen, K., Baluteau, J-P., Pouliquen, D., Ferand, D., Dargent, P., Michel, G., Martignac, J., Rodriguez, L., Jennings, D.E., Caldwell, M.E., Richards, A.G., Hamilton, P.A., Naylor, D.A., *FIRST-SPIRE spectrometer: a novel imaging FTS for the submillimeter* in UV, Optical, and IR Space Telescopes and Instruments, Eds. J.B. Breckinridge and P. Jakobsen, Proc. SPIE **4013**, 196-207, 2000.

10. Swinyard, B.M., Dohlen, K., Ferand, D., Baluteau, J-P., Pouliquen, D., Dargent, P., Michel, G., Martignac, J., Ade, P.A.R., Hargrave, P.C., Griffin, M.J., Jennings, D.E., Caldwell, M., *Imaging FTS for Herschel SPIRE*, in IR Space Telescopes and Instruments. Ed. J.C. Mather, Proc. SPIE, **4850**, 698-709, 2003.

11. Bianchini, G., Cortesi, U., Palchetti, L. and Pascale, E., *Cosmic-ray spikes localization and correction in FT spectrometer data*, Infrared Physic and Technology, **43**, 33-38, 2002.

12. Woodcraft, A.L., Sudiwala, R.V., Wakui, E., Ade, P.A.R., Griffin, M.J., Bhatia, R.S., Bock, J.J., Lange, A.E., Turner, A.D., Yun, M.H. and Beeman, J.W., *Predicting the response of a sub-mm bolometer to cosmic rays*, Appl. Opt., **42**, 5009-5016, 2003.

13. Devlin, M.J., *The Balloon-Borne Large Aperture Submillimeter Telescope*, in Millimeter and Submillimeter Detectors for Astronomy II, Eds. J. J. Zmuidzinas, W. S. Holland and S. Withington , Proceedings of SPIE, **5498**, (in press) 2004.

14. Norton, R.H. and Beer, R., *New apodizing functions for Fourier spectrometry*, J. Opt. Soc. Am., **66**, 259-264, 1976.

15. Naylor, D.A. and Tahic, M.K., Applied Optics, *in preparation*.

16. Filler, A.H., *Apodization and interpolation in Fourier transform spectroscopy*, J. Opt. Soc. AM., **54**, 762-767, 1964.

17. Cooley, J.W. and Tukey, J.W., *An algorithm for the machine calculation of complex Fourier series*, Maths. Comput. **19**, 297-301, 1965.

18. Brault, J.W., *New approach to high-precision Fourier transform spectrometer design*, App. Opt., **35**, 2891-2896, 1996.

19. Yang, H., Griffiths, P.R. and Mannin, C.J., *Improved data processing by application of Brault's method to ultra-rapid-scan FT-IR spectrometry*, Applied Spectroscopy, **56**, 1281-1288, 2002.

20. Duijndam, J.W. and Schonewille, M.A., *Nonuniform fast Fourier transform*, Geophysics, **64**, 539-551, 1999.

21. Potts, D., Steidl, G. and Tasche, M., *Fast Fourier transform as nonequispaced datas*, in: Modern Sampling Theory: Mathematics and Applications, J.J. Benedetto and P.J.S.G. Ferreira (Eds.), Birkhauser Boston, Applied and Numerical Harmonic Analysis Series, Chapter 12, 249-274, 2001.

22. http://www.math.uni-luebeck.de/potts/nfft/

23. Pelt, J., *Fast computation of trigonometric sums with applications to frequency analysis of astronomical data*, in D. Maoz, A. Sternberg and E.Leibowitz, (Eds) Astronomical Time Series, Kluwer Academic Publishers, 179-182, 1997.

24. "The Interactive Data Language", Research Systems Inc., 4990 Pearl East Circle, Boulder, CO, 80301, USA.

25. Press, W.H., Teukolsky, S.A., Vetterling, W.T., and Flannery, B.P., *Numerical Recipes in C (2nd ed.): The Art of Scientific Computing,* Cambridge University Press, New York, 1992.

26. More, J. and Wright, S., *Optimization Software Guide,* Frontiers in Applied Mathematics, Published by the Society for Industrial and Applied Mathematics, **14**, 1993.